Environmental Science: Atmospheres

ROYAL SOCIETY OF CHEMISTRY

PAPER

View Article Online
View Journal | View Issue



Cite this: *Environ. Sci.: Atmos.*, 2024, **4**, 252

# Improving model representation of rapid ozone deposition over soil in the central Tibetan Plateau†

Chong Zhang,[a] Jianshu Wang,[a] Yingjie Zhang,[‡a] Wanyun Xu,[b] Gen Zhang,[b] Guofang Miao,[c] Jiacheng Zhou,[d] Hui Yu,[d] Weixiong Zhao,[d] Weili Lin,[e] Ling Kang,[a] Xuhui Cai,[a] Hongsheng Zhang[f] and Chunxiang Ye[*a]

Ozone soil deposition contributes a major part to the total deposition of ozone on land covered by low vegetation and perturbs the ozone budget on both regional and global scales. Large model-observation divergences in ozone soil deposition require continuous efforts to improve the mechanical understanding and model representation. Observation of ozone deposition over bare soil directly meets the requirement. Here, we performed field observation of ozone deposition over bare soil first available in the Tibetan Plateau (TP) using the aerodynamic gradient method. A top ozone deposition velocity with a daily mean of 0.49 ± 0.11 (1 sd) cm $s^{-1}$ (1 May to 10 July 2019) and an hourly mean maximum across the diel pattern of 0.73 ± 0.67 cm $s^{-1}$ in the afternoon were recorded. Such rapid ozone deposition was mainly attributed to extremely low soil resistance ($R_{soil}$), which was further regulated by median low soil clay content, dry conditions, and strong solar radiation in the central TP. Parameterization of $R_{soil}$ in the newly developed Stella scheme was demonstrated to be effective according to our verification. An updated scheme was further attained with the inclusion of our observation and better represents the $R_{soil}$ variability than the Stella scheme. More verification is therefore encouraged and hopefully to improve the Stella scheme. Finally, both the Stella scheme and our updated scheme showed great advantages over the oversimplified scheme in current models and should be considered more seriously for the sake of better representation of ozone soil deposition and its variability.

Received 25th October 2023
Accepted 30th December 2023

DOI: 10.1039/d3ea00153a

rsc.li/esatmospheres



## Environmental significance

Tropospheric ozone is an important gaseous pollutant and a short-lived climate forcer that affects air quality, human health and climate. Ozone soil deposition represents a non-negligible fraction of ozone budget. However, it is highly underestimated by current models and therefore leads to ill-representation of ozone distribution. To explore the soil deposition mechanism and improve the model representation, we performed direct measurements of ozone deposition velocity on bare soil in the central Tibetan Plateau (TP), an ideal experimental field for its pristine nature in terms of weak human perturbation on both land use and ozone photochemistry. For the first time, our measurement recorded in the TP the top ozone deposition velocity on soil, which could be accounted for by measured meteorological and edaphic parameters. An updated parameterization scheme based on Stella *et al.* was summarized and better represented ozone deposition velocity and its environmental variability, relative to the schemes commonly used in chemical transport models. The Stella scheme is therefore worthy of more serious consideration for the sake of better representation of ozone soil deposition and its variability. Our data has also confirmed that ozone soil deposition in the TP is underestimated by current model evaluations.

[a]*SKL-ESPC & SEPKL-AERM, College of Environmental Sciences and Engineering and Center for Environment and Science, Peking University, Beijing, China. E-mail: c.ye@pku.edu.cn*

[b]*State Key Laboratory of Severe Weather & Key Laboratory for Atmospheric Chemistry of CMA, Institute of Atmospheric Composition, Chinese Academy of Meteorological Sciences, Beijing, China*

[c]*School of Geographical Sciences, Fujian Normal University, Fuzhou, China*

[d]*Laboratory of Atmospheric Physico-Chemistry, Anhui Institute of Optics and Fine Mechanisms, Chinese Academy of Science, Hefei, Anhui, China*

[e]*College of Life and Environmental Sciences, Minzu University of China, Beijing, China*

[f]*Department of Atmospheric and Oceanic Sciences, School of Physics, Peking University, Beijing, China*

† Electronic supplementary information (ESI) available. See DOI: https://doi.org/10.1039/d3ea00153a

‡ School of Ecology and Nature Conservation, Beijing Forestry University, Beijing, China.

## 1 Introduction

Tropospheric ozone is an important gaseous pollutant and a short-lived climate forcer that plays a key role in atmospheric oxidative capacity, oxidative damage to humans and vegetation, and climate change.[1–4] Obtaining accurate temporal and spatial variability of ozone is essential for assessing its role. While dense ozone measurement networks have been established in the United States, Europe, and eastern Asia, and great progress has been made in China in recent years, observational constraints on ozone are still absent in other regions, especially in background areas globally.[5] Chemical transport models (CTMs) are alternative tools to evaluate the temporal–spatial

variability in ozone in those regions where measurement is absent. Simulations of ozone by CTMs are numerical approximations of the budgets of ozone, including chemical reactions that lead to ozone formation and destruction, tropospheric influx from stratosphere–troposphere exchange, deposition loss, and convectional and advectional transport. However, the simulation representations are limited by our current incomplete understanding of and parameterization methods for these budget items.[6]

Simulation representation of tropospheric ozone, especially ozone at the surface, is sensitive to the representation of ozone dry deposition.[7–11] The resistance-analogy parameterization framework for ozone deposition developed by Wesely,[12] is widely accepted by different deposition schemes to explain and parameterize ozone deposition on various land cover types.[13–18] Briefly, the resistance analogy framework conceptualized the dry deposition of ozone or other pollutants as a three-step process including (1) ozone transport downward to a given surface by atmospheric turbulence, (2) mass transfer through the quasi-laminar sublayer around the interface of air and the surface, and (3) uptake on the surface. The ozone deposition velocity, $v_d$, can be expressed as the reciprocal of the total mass transfer resistance of these three-step processes, namely, aerodynamic resistance $R_a$, quasi-laminar sublayer resistance $R_b$, and surface resistance $R_c$.[12]

Studies comparing different deposition schemes at site-specific sites illustrate that the representation of $R_c$ and its variability cause the largest differences of $v_d$.[19,20] Among different deposition schemes, $R_a$ is typically modelled with different empirical formulae of the Monin–Obukhov similarity theory (MOST), and $R_b$ is modelled with a same formula. Wu *et al.*[19] compared $R_a + R_b$ over a forest modelled by four different MOST-based models and found similar results. Combined with the relatively smaller contribution of $R_a + R_b$ than $R_c$ to the total resistance (see Section 3.2 below), more attention is focused on the parameterization of $R_c$. The parameterization of $R_c$ used in the resistance analogy considers the resistance of ozone uptake by stomatal, cuticular, and ground surfaces, the last of which mainly refers to soil surfaces. Relatively intensive field observations of ozone deposition have been performed over developed canopies.[21–28] Canopy related stomatal and cuticular uptake are the main ozone deposition paths in these observations. However, studies on crops found that the determining role of stomatal and cuticular resistances highly depends on canopy development and abundance.[29,30] On surfaces with lower and sparser canopies, such as growing croplands and grasslands, soil resistance ($R_{soil}$) could contribute up to 55% to total ozone deposition resistance; thus, $v_d$ is more sensitive to $R_{soil}$ for these land cover types.[31,32]

Ozone soil deposition contributes heavily to the global budget of ozone deposition because a considerable fraction of global land cover is desert, bare soil, and sparse vegetation. However, the modeling of ozone soil deposition remains highly uncertain. Gross model underestimation of ozone deposition on bare soil (equivalent to ozone soil deposition) was consistently found.[33,34] The large discrepancy of ozone soil deposition and its variability between measurements and simulations implies the poor representations of ozone soil deposition by current CTMs. The poor representation is mainly attributed to the oversimplified $R_{soil}$ parameterization scheme that uses two-level prescribed values for dry and wet surfaces without more complex response relationships with soil moisture, soil temperature or soil clay content.[19] Modification attempts have been made with the aim of enabling model power to better describe the variability in $R_{soil}$. Either a positive dependence of $R_{soil}$ on soil moisture or a negative dependence on temperature was reported based on site-specific observations, but the expressions between $R_{soil}$ and moisture or temperature should not be extrapolated to other sites.[35–37] A few studies introduced a universal corrected function of soil moisture or temperature based on mathematical assumptions; however, field observation validation is rare.[7,38] Stella *et al.*[33,34] summarized their six field observations over bare soil and proposed a dual-parameter semiempirical $R_{soil}$ parameterization (known as the "Stella scheme") involving soil clay content and surface relative humidity ($RH_{surf}$). In the Stella scheme, $RH_{surf}$ is believed to better represent the varied and complex effect of meteorological parameters, such as surface temperature ($T_{surf}$), soil moisture, and solar radiation. Soil clay content, as a second influencing factor, reasonably accounts for the spatial heterogeneity of soil uptake reactivity toward ozone and therefore $R_{soil}$.

Although the Stella scheme seems to have the potential to describe $R_{soil}$ and its variability, limited field observational validation hinders direct extrapolation or CTMs inclusion. The observations of ozone soil deposition were mostly conducted over agricultural fields after harvest to avoid interference of the canopy.[33] However, frequent agricultural activities, such as plowing, fertilization, and irrigation, can cause transformations in surface soil physics and chemical characteristics and potentially soil uptake reactivity toward ozone. Additionally, strong $NO_x$ and/or VOCs emissions from agricultural soil can participate in the fast atmospheric chemical conversion of ozone and therefore significantly interfere with the measurement of ozone soil deposition.[42,43] Field observation of ozone deposition in environments with negligible NO or highly reactive VOCs sources is ideal in terms of less chemistry interference and human activity perturbation of soil but is sporadically available.[33] In addition, $R_{soil}$ is highly affected by soil clay contents and hydrothermal conditions based on the previous summary, which are spatially heterogeneous in different climate regions. Previous observations were performed mostly in subtropical climate regions. Field observations in more climate regions are therefore highly demanded (Fig. 1). The TP is a typical highland climate region where both soil clay content and moisture are expected to be different from the subtropical climate regions. And TP is characterized as a highly pristine area and covered with sparse and low vegetation, implying weak perturbation of land use and ozone chemistry on ozone soil deposition.

The @Tibet series field campaign supports ozone deposition measurement over the Tibetan Plateau (TP). In this study, we took advantage of the ideal experimental field and performed the first measurement of ozone deposition velocity on bare soil in the TP, acquired from the aerodynamic gradient method. The

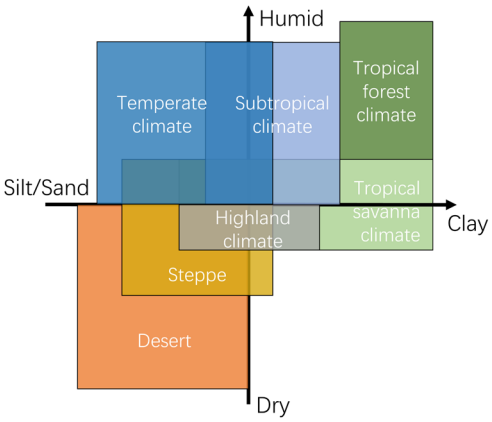


Fig. 1 Simplified concept of climatic regions with different soil clay contents and hydrothermal conditions. Previous measurements of soil resistance ($R_{soil}$) have been conducted mostly in subtropical climate regions in the figure. Data of climate classification is from Chen *et al.*[39] Soil clay content data is from Harmonized World Soil Database v2.0.[40] Humidity data is referenced to Kummu *et al.*[41]

aims of this study are (i) to measure $v_d$ in the TP and to identify the factors controlling $v_d$ and $R_{soil}$ and (ii) to evaluate and improve the Stella scheme by inclusion of our verifications.

## 2 Methods

### 2.1 Measurements

The field measurement of ozone deposition was performed from 1 May to 10 July 2019 at Nam Co Comprehensive Observation and Research Station, Chinese Academy of Sciences (CAS) (NMC site, 30°46.30′N, 90°59.31′E, 4730 m a.s.l.), as an essential part of the @Tibet 2019 campaign. Due to power outages, instrument malfunctions and other factors, the valid data cover 50 days. Detailed descriptions of NMC site and @Tibet 2019 campaign can be found in previous studies.[44–46] NMC site is located in an open flat field ~1 km southeast of Nam Co Lake and more than 15 km to the north and west of the Nyainqêntanglha Mountains. In addition, a sublake of Nam Co Lake is ~280 m away from the site. NMC site is characterized by a continental background of the atmosphere with few surrounding populations, and isolated from Lhasa, the largest city in the TP.

High-altitude and mountainous environment results in a typical arctic–highland climate of this area. The monthly mean air temperature ranges from −7.8 °C to 12.2 °C, and solar radiation reaches 1200 W m$^{-2}$ in May.[47] Annual precipitation of approximately 400 mm is concentrated during the Asian Summer Monsoon (ASM) period from June to September.[48] In this cold and arid area, the soil is poorly developed because of sporadic vegetation coverage and weak chemical weathering, which is embodied in a loose soil structure and low clay content.[49]

Air temperature and relative humidity (HMP155A, Vaisala, FI) and wind speed (010C, Met One, USA) profiles were measured at 1.8, 3.8, and 5.8 m height, and wind direction (020C, Met One, USA) was measured at 5.8 m. Solar radiation, including incoming and reflected shortwave and longwave radiation (CNR4, Kipp & Zonen, NL) and j($NO_2$) (ultrafast CCD-detector spectrometer, Metcon, GER), were measured. Soil temperature and soil water content (CS655, Campbell Scientific Inc., USA) profiles were also measured at 5, 15, and 25 cm below ground. $NO_2$ concentration was measured by a sensitive incoherent broadband cavity enhanced absorption spectroscopy $NO_2$ analyzer.[50] As the NO concentration was too low to be measured, photostationary state calculation of the NO concentration (NO_PSS) was carried out with measured $O_3$, $NO_2$, and $j(NO_2)$.

Ozone flux was measured using the aerodynamic gradient (AG) method, with characterization of the micrometeorological environment by the eddy covariance (EC). The AG method is based on *K*-theory, an application of MOST. Similar to Fick's Law, the *K*-theory assumes that the turbulence flux can be expressed as the product of the turbulence exchange coefficient *K* and vertical concentration gradient. Therefore, the ozone flux can be calculated as follows:

$$F = -K\frac{\mathrm{d}[O_3]}{\mathrm{d}Z} \quad (1)$$

where *F* is the ozone flux (ppbv m s$^{-1}$ or nmol m$^{-2}$ s$^{-1}$), *K* is the turbulence exchange coefficient (m$^2$ s$^{-1}$), and $\frac{\mathrm{d}[O_3]}{\mathrm{d}Z}$ is the vertical ozone gradient between the two measurement heights (ppbv m$^{-1}$ or nmol m$^{-2}$). A UV photometric ozone analyzer (Model 49i, Thermo-Environmental Instruments Inc., USA) measured the ozone concentration. Air was sampled at 6.8 m and 1.8 m of the tower through a 27 m Teflon sampling tube with sequential sampling in a 30 min duty cycle. A solenoid valve was used to control the measurement time of 15 min at each height. The measurement gap of 15 min at each height was filled by linear interpolation of adjacent data at the same height. Therefore, continuous ozone gradient was obtained. The sampling tube was covered by black foam for heat preservation and light shading. *K* is calculated as follows:[51]

$$K = \kappa u_*(z_2 - z_1)\left[\ln\frac{z_2 - d}{z_1 - d} - \psi_h\left(\frac{z_2 - d}{L}\right) + \psi_h\left(\frac{z_1 - d}{L}\right)\right] \quad (2)$$

where $\kappa$ is von Karman's constant (0.4), $u_*$ is the friction velocity (m s$^{-1}$), $z_1$ and $z_2$ are the lower and greater heights of ozone measurement respectively (m), *d* is the zero-plane displacement height (m), *L* is the Obukhov length (m), and $\psi_h(z/L)$ is the integrated stability correction function for heat:

$$\psi_h(z/L) = \begin{cases} 2\ln\left(\frac{1+y}{2}\right), & z/L < 0 \\ -5z/L, & z/L > 0 \end{cases} \quad (3)$$

where $y = (1 - 16z/L)^{1/2}$. As EC is a reliable method to characterize atmospheric turbulence, $u_*$ and L were provided by the EC method and used in the AG method. The EC method was also used to measure fluxes of momentum, sensible heat (*H*), latent heat (LE), water vapor, and $CO_2$. The EC system includes an integrated $CO_2$/$H_2O$ open-path gas analyzer and 3D sonic anemometer (IRGASON, Campbell Scientific Inc., USA), electronics for synchronizing gas and wind data (EC100, including

a temperature thermistor probe and a barometer, Campbell Scientific Inc., USA), and a data logger (CR3000, Campbell Scientific Inc., USA). The IRGASON was mounted at 6.8 m. Data were sampled and recorded at 10 Hz and processed by EddyPro software (version 7.0.8, LiCor, USA) for a 30 min flux averaging interval. Standard data processing methods were used, including spike removal, double axis rotation, linear detrending, humidity correction of sonic temperature, WPL correction and spectral correction.[52] Quality checks of raw data and flux results were also performed. The footprint was estimated by the Kljun *et al.*[53] method.

Ozone deposition velocity can be determined as follows:

$$v_d = -\frac{F}{[O_3]} \times 100 \quad (4)$$

where $v_d$ is the ozone deposition velocity (cm $s^{-1}$), and $[O_3]$ is the average concentration of ozone between two measurement heights (ppbv).

### 2.2 Resistance analogy

The resistance analogy method describes the mechanism and kinetics of ozone deposition. It also provides a numerical model representation of $v_d$. By considering that the reciprocal of $v_d$ is the total resistance to mass transfer, the influence of the above mentioned three processes on $v_d$ can be expressed in terms of the following electrical analogy:

$$v_d = \frac{1}{R_{all}} = \frac{1}{R_a + R_b + R_c} \quad (5)$$

$R_c$ consists of the resistances of these different surfaces, such as soil, leaf cuticular or ice. As the surface at the study area of NMC site is bare soil, $R_c$ in this study is equal to the soil resistance $R_{soil}$. $R_a$ and $R_b$ are calculated as follows:

$$R_a(z) = (\kappa u_*)^{-1}\left[\ln\frac{z}{z_0} - \psi_h(z/L) + \psi_h(z_0/L)\right] \quad (6)$$

$$R_b(O_3) = 2(\kappa u_*)^{-1}(S_c/P_r)^{2/3} \quad (7)$$

where $z$ is the reference height (mean ozone measurement height, m), $z_0$ is the roughness length for momentum (m), $S_c$ is the Schmidt number, and $P_r$ is the Prandtl number for air (0.72).

### 2.3 Calculation of surface parameters

Temperature and moisture at the surface, $T_{surf}$ and $RH_{surf}$, instead of atmospheric or edaphic parameters, are recommended as measures of temperature and moisture conditions of soil uptake of ozone by Stella *et al.*[34] and have shown less variability than other measures. Thus, the same scheme is used in this study following the calculation method in Stella *et al.*:[32]

$$T_{surf} = \frac{H(R_a(z) + R_b)}{\rho C_p} + T_a \quad (8)$$

$$\chi_{H_2O,\,surf} = E(R_a(z) + R_{b,H_2O}) + X_{H_2O,\,a} \quad (9)$$

$$P_{vap,surf} = \frac{\chi_{H_2O,surf} R(T_{surf} + 273.15)}{M_{H_2O}} \quad (10)$$

$$P_{sat}(T_{surf}) = P\exp\left[\frac{M_{H_2O}10^{-3}\gamma}{R}\left(\frac{1}{T_0 + 273.15} - \frac{1}{T_{surf} + 273.15}\right) \times\right] \quad (11)$$

$$RH_{surf} = \frac{P_{vap,surf}}{P_{sat}(T_{surf})} \times 100 \quad (12)$$

where $\rho$ is the air density (kg $m^{-3}$), $C_p$ is the air specific heat (J $kg^{-1}$ $K^{-1}$), $\chi_{H_2O,surf}$ and $X_{H_2O,a}$ are the air concentration of water (g $m^{-3}$) at the surface and reference height, respectively, $X_{H_2O,a}$ is calculated from the air relative humidity, $E$ is the water vapor flux (kg $m^{-2}$ $s^{-1}$), $P_{vap,surf}$ is the water vapor pressure at the surface (Pa), $R$ is the universal gas constant (J $mol^{-1}$ $K^{-1}$), $M_{H_2O}$ is the molecular weight of water (g $mol^{-1}$), $P_{sat}(T_{surf})$ is the saturation vapor pressure at $T_{surf}$ (Pa), $P$ is the atmospheric pressure (Pa), $\gamma$ is the latent heat of vaporization of water (J $kg^{-1}$), and $T_0$ is the boiling temperature of water at $P$ (°C).

### 2.4 Data quality assurance

The use of the AG method requires some prerequisites, such as stationary but strong enough turbulence, no chemical interference and uniform underlying surface.

First, the AG method under extremely unstable and stagnant conditions were thought to suffer from large uncertainties due to the invalidation of MOST. The ratio of the measurement height and the Obukhov length ($z/L$) is used to evaluate the atmospheric stability. $z/L$ between −2 and 1 are required. Valid data coverage was 79% with a 30 min time resolution.

Second, the NO titration of ozone, which might cause a substantial surface gradient of ozone, is often regarded as an uncertainty source in ozone flux measurements in some areas.[43] As ozone titration by a considerable NO near the surfaces in agricultural fields could occur in minutes, it might compete with the vertical transport of ozone in determining the surface gradient of ozone. A comparison between the turbulence transport time ($\tau_{trans}$) and the chemical reaction time ($\tau_{chem}$) can be used to evaluate the influence of the chemical reaction on the ozone flux. Following the method of Stella *et al.*,[34] the $\tau_{trans}$ can be expressed as the transfer resistance through each layer multiplied by the layer height. The layer height of the quasi-laminar boundary layer, $(z_0 - z_{0'})$, is so small that the contribution of the quasi-laminar boundary to $\tau_{trans}$ is negligible. $\tau_{chem}$ is calculated as the lifetime of ozone reacting with NO.

$$\tau_{trans} = R_a \times (z_m - z_0) + R_b \times (z_0 - z_{0'}) = R_a \times z_m \quad (13)$$

$$\tau_{chem} = \frac{1}{\chi_{NO}(z_m) \times k_r} \quad (14)$$

where $z_m$ is the measurement height, $\chi_{NO}(z_m)$ is the concentration of NO_PSS (ppbv) at the measurement height. The

reaction rate constant ($k_r$ in ppbv$^{-1}$ s$^{-1}$) is calculated as $k_r = 0.0444 \times \exp(-1370/(T_a + 273.15))$.[54] NMC site is almost free from interference from anthropogenic emissions due to the extremely low value of NO_PSS with an average of only 58 pptv. $\tau_{chem}$ is calculated to be 10-fold that of $\tau_{trans}$ (Fig. S1a†), suggesting that this chemical perturbation of the ozone flux measurement is negligible at NMC.

Third, the footprint area of the ozone flux measurement shows *ca.* 3% attribution to the water surface to the west of our measurement site 280 m away (Fig. S1b†). Ozone deposition on the water surface was roughly evaluated based on the turbulence measurement and typical water surface resistance for ozone uptake of 1000 s m$^{-1}$. The calculated value of $v_d$ is 1/4–1/8 of that on soil. However, considering the contribution of the water surface to the footprint area, corrections of less than 3% for ozone flux measurement are thus abandoned.

The ozone flux is determined from the product of $K$ and $\frac{d[O_3]}{dZ}$ (eqn (1)), thus the uncertainty of ozone flux includes the uncertainty of these two factors, $\sigma_K$ and $\sigma_{(d[O_3]/dZ)}$. $\sigma_K$ contains uncertainty from measurements and those arising from the parameterization (eqn (2) and (3)), both of which have larger uncertainty under stable atmospheric conditions, *i.e.* during nighttime. Quantify of $\sigma_K$ is tough[55] and out of our scope. Constant relative uncertainties of 20% and 50% are given to $K$, which is robust.[55,56] To validate the estimation of $\sigma_K$, we compared $H$ and LE derived separately from the EC method and AG method. It was indicated that the diel profiles were similar, and the magnitudes of $H$ and LE were comparable between the two methods (Fig. S1c and d†). The AG method overestimated $H$ by approximately 10%, and biased LE by a constant systematic error of approximately 18 W m$^{-2}$ compared to the EC method. Further examination of the temperature and moisture gradients suggested that inconsistencies between different hygrothermometers might account for the divergences.

$\sigma_{(d[O_3]/dZ)}$ is determined by the uncertainty of the difference of ozone concentration $\sigma_{\Delta[O_3]}$, because measurement of height is accurate. Ozone concentration at two heights were measured by one ozone analyzer and thus $\sigma_{\Delta[O_3]}$ is equal to $2\sigma_{[O_3]}$, which supposed to be 0.35 ppbv. Whether the ratio $\frac{\Delta[O_3]}{\sigma_{\Delta[O_3]}}$ larger than 1 is used to judge whether $\Delta[O_3]$ is significant. 10% of ozone gradient data were insignificant but still retained to avoid a misestimation of the average flux. It is noteworthy that linear interpolation of the 15 min ozone measurement gaps could be an uncertainty source to the ozone gradient but could not be accurately evaluated. Extreme and unreasonable values of the ozone gradient occasionally appeared from the interpolation method. However, it was plausible to see a typical diel variation of the ozone gradients (Fig. S1e†). Therefore, to reduce the impact of outliers on the analysis, outlier spikes of $v_d$ and maximal or minimal 2.5% of $R_{soil}$ are excluded from the data analysis.

Using Gaussian uncertainty propagation, the uncertainty of ozone flux and ozone deposition velocity could be calculated as follows:

$$\frac{\sigma_F}{F} = \sqrt{\left(\frac{\sigma_K}{K}\right)^2 + \left(\frac{\sigma_{(d[O_3]/dZ)}}{(d[O_3]/dZ)}\right)^2} \approx \sqrt{\left(\frac{\sigma_K}{K}\right)^2 + \left(\frac{\sigma_{\Delta[O_3]}}{\Delta[O_3]}\right)^2} \quad (15)$$

$$\frac{\sigma_{v_d}}{v_d} = \sqrt{\left(\frac{\sigma_F}{F}\right)^2 + \left(\frac{\sigma_{[O_3]}}{[O_3]}\right)^2} \quad (16)$$

$\frac{\sigma_F}{F}$ were dependent on $\frac{\sigma_K}{K}$ during nighttime and dependent on both $\frac{\sigma_K}{K}$ and $\frac{\sigma_{\Delta[O_3]}}{\Delta[O_3]}$ during daytime. Diel $\frac{\sigma_F}{F}$ varies from 25.7% during daytime to 51.1% during nighttime, with an average of 39.8%. As $\frac{\sigma_{[O_3]}}{[O_3]}$ is less than 1%, $\frac{\sigma_{v_d}}{v_d}$ is approximately equal to $\frac{\sigma_F}{F}$.

### 2.5 Simulation of ozone deposition velocity with different $R_{soil}$ parameterizations

The resistance analogy with the Stella scheme (hereafter called RA_SS) is performed to evaluate the reproducibility of $v_d$. $R_a$ and $R_b$ are calculated by eqn (6) and (7) with meteorological parameters measured on site. The expression of the Stella scheme is as follows:

$$R_{soil} = R_{soil\ min} \times e^{(k \times RH_{surf})} \quad (17)$$

$$R_{soil\ min} = 702 \times (\text{clay content})^{-0.98} \quad (18)$$

$$k = 0.0118\, e^{0.0266 \times (\text{clay content})} \quad (19)$$

where $R_{soil\ min}$ (s m$^{-1}$) is the soil resistance when $RH_{surf}$ is 0%, $k$ (unitless) is the coefficient of the exponential function, and clay content (%) is the fraction of clay content in the topsoil. The soil clay content of NMC site, 14.5%, is obtained from the soil dataset by Ito and Wagai.[57]

## 3 Results and discussion

### 3.1 Environmental conditions and ozone deposition velocity

The environmental conditions of ozone deposition are largely determined by climate regions. As a typical highland mountain climate region, NMC site features strong solar radiation and cold, arid, and windy meteorological conditions. The measurements covered two periods with distinct meteorological parameters, namely, the premonsoon period before 1 July and the ASM period after 1 July (shaded area in Fig. S2†). In the premonsoon period, solar radiation ($R_g$) at NMC site was even larger than the solar constant (1367 W m$^{-2}$) at cloudless noon (Fig. S2a†), with a maximum of 1552.6 W m$^{-2}$ on 11 June. However, with such strong $R_g$, air temperature ($T_a$) is quite low due to the buffering effect of plateau permafrost and could be below 0 °C in early May (Fig. S2b†). $T_a$ slowly increased from 4.3 ± 4.3 °C to 11.8 ± 4.0 °C in the premonsoon period. Under the additive effects of low soil water content (SWC) and strong $R_g$, typical air relative humidity ($RH_a$) was lower than 25% during the daytime in the premonsoon period (Fig. S2c†). Strong winds occurred frequently, and the wind speed (WS) exceeded 10 m s$^{-1}$ on some days (Fig. S2d†). In the ASM period, the ASM brought abundant moisture to the TP and resulted in more frequent precipitation. $R_g$ showed a dramatic decline compared

 

to the premonsoon period, but it still remained at a high level compared with regions of the same latitude. Volumetric soil water content (SWC) zoomed from 0.01 to 0.2 after 1 July. Weakened $R_g$ and enhanced SWC in the ASM period caused a slight decrease in $T_a$ and a significant increase in $RH_a$. WS showed obvious differences from the premonsoon period, with the peak dropping, but WS mean at night increased.

Diel pattern of key parameters that related to calculation of $R_a$, $R_b$, $R_{soil}$ and derivation of $v_d$ according to eqn (6)–(12) and (17) are performed in Fig. 2. Over the entire observation period, the hourly mean $T_a$ ranged from 1.6 ± 4.6 °C at night to 10.6 ± 4.3 °C in the daytime (Fig. 2b). Significant enhancements of $T_{surf}$ compared to $T_a$ occurred with a maximal hourly enhancement of 15.6 °C during daytime. This was caused by strong $R_g$, of which the hourly mean maximal reached 1252.4 ± 348.5 W

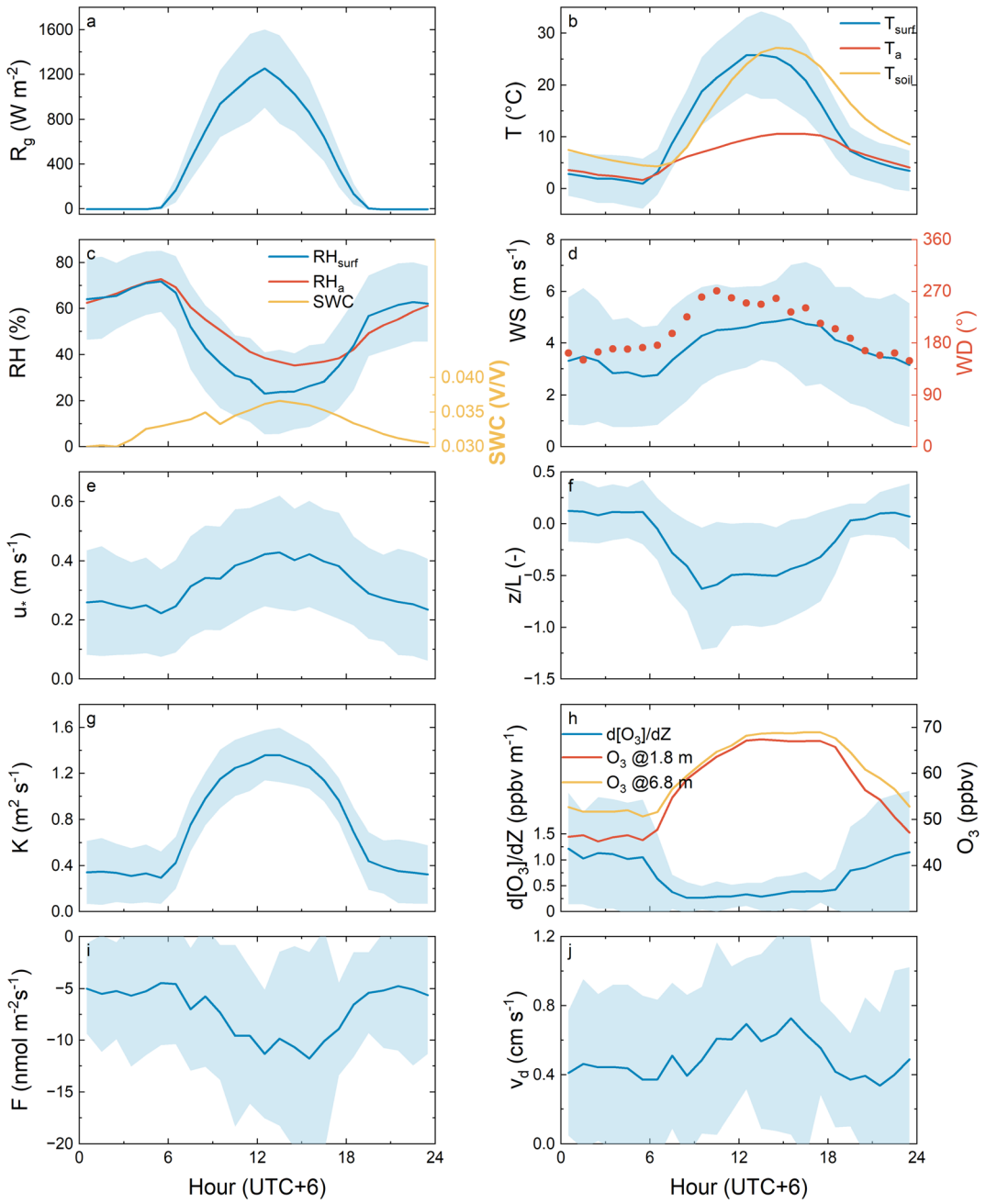


Fig. 2 Diel pattern of meteorological parameters and edaphic parameters associated with ozone deposition velocity derivation and deposition resistance derivation. Diel pattern of (a) solar radiation ($R_g$), (b) air temperature at 1.8 m ($T_a$), surface temperature ($T_{surf}$) and soil temperature at −5 cm ($T_{soil}$), (c) air relative humidity at 1.8 m ($RH_a$), surface relative humidity ($RH_{surf}$) and soil water content (SWC), (d) wind speed at 1.8 m (WS) and wind direction (WD), (e) friction velocity ($u_*$), (f) atmospheric stability criterion ($z/L$), (g) turbulence exchange coefficient ($K$), (h) gradient of ozone between 6.8 m and 1.8 m (d[$O_3$]/d$Z$), ozone concentration at 6.8 m and ozone concentration at 1.8 m, (i) ozone flux ($F$), and (j) ozone deposition velocity ($v_d$). The solid line is the diel mean, and the shading is variation of our observations.

$m^{-2}$ (Fig. 2a and b). The enhancement of $T_{surf}$ further caused lower $RH_{surf}$ according to eqn (12). $RH_{surf}$ at noon was as low as 23.2 ± 17.8%, which is 15.3% of decrease compared with $RH_a$ (Fig. 2c). The increased $T_{surf}$ and consequently decreased $RH_{surf}$ may result in a small $R_{soil}$, and thus favors ozone deposition.

Solar radiation and wind supply energy to atmospheric turbulence which affects $R_a$ and $R_b$. A campaign average $R_g$ of 411.9 ± 469.2 W $m^{-2}$ and wind speed of 3.83 ± 0.72 m $s^{-1}$ (Fig. 2a and d) favored strong atmospheric turbulence. The influence of solar radiation and wind on atmospheric turbulence strength is reflected in the diel pattern of friction velocity ($u_*$) and $z/L$ (Fig. 2e and f). $u_*$ remained fairly large throughout the day with a maximum of 0.43 ± 0.19 m $s^{-1}$ around noon. The mean $u_*$ during the night dropped to 0.2 m $s^{-1}$. An opposite diel trend was shown in $z/L$, with an average of 0.1 at night and −0.5 in the daytime. A nighttime $z/L$ of 0.1 also confirmed that the atmospheric stability at night was nearly neutral and did not seriously block the development of turbulence. Active atmospheric turbulence resulted in rapid vertical turbulence transport, which was characterized by $K$ (eqn (2), (3), and Fig. 2g). The diel pattern of $K$ is similar to those of WS and $R_g$. Nighttime $K$ remained at approximately 0.3–0.4 $m^2$ $s^{-1}$, while $K$ increased to 1.36 ± 0.24 $m^2$ $s^{-1}$ at noon. It can be inferred from the diel pattern of $K$ and $R_g$ that surface heating driven by solar radiation plays a dominant role in turbulence development at NMC site.

$F$ and $v_d$ are determined based on the $K$, as well as the measurements of $d[O_3]/dZ$ between 6.8 m and 1.8 m (eqn (1) and (4)). The ozone measured at the two heights showed similar diel profiles but distinct abundances (Fig. 2h). The ozone at 1.8 m ranged from 45.6 ± 11.4 ppbv at night to 67.4 ± 10.4 ppbv in the daytime, with a mean of 56.9 ± 8.6 ppbv. The ozone at 6.8 m ranged from 50.7 ± 12.1 ppbv at night to 69.0 ± 10.3 ppbv in the daytime, with a mean of 60.2 ± 7.0 ppbv. A similar diel profile of $F$ was derived compared to that of $K$, WS, and $R_g$ (Fig. 2i). Negative values suggested a downward deposition of ozone. The daily mean $F$ was −7.09 ± 2.36 nmol $m^2$ $s^{-1}$, with a noontime maximum of −11.78 ± 10.28 nmol $m^2$ $s^{-1}$. As the low air pressure counteracts high volume concentrations of ozone to $F$, the large $F$ could be explained mainly by high $v_d$. $v_d$ showed a bridge-shaped diel profile (Fig. 2j) with the mean of 0.49 ± 0.11 cm $s^{-1}$ and a noontime peak of 0.73 ± 0.67 cm $s^{-1}$. The $v_d$ observed here is comparable to typical $v_d$ in forests and one of the highest previously reported over bare soils.[33,58,59] Notably, a high nighttime $v_d$ of approximately 0.4 cm $s^{-1}$ is observed, which is among the top values ever reported.[33] Although nighttime $v_d$ has larger uncertainty than that of daytime, quite high $u_*$ and $z/L$ much less than 1 during nighttime favored high nighttime $v_d$ at NMC.

### 3.2 Determinative role of $R_{soil}$ in ozone deposition and its variability

The constitution of deposition resistance provides the information to explain the magnitude of $v_d$ and its diel variation. The diel profile of deposition resistance and its components is shown in Fig. 3a. The deposition resistance of ozone, $R_{all}$, showed a typical U-shaped diel profile, which accounts for the bridge-shaped $v_d$. Both $R_{soil}$ and $R_a$ + $R_b$ showed a typical U-shaped diel profile as well. The daytime low $R_{soil}$ at NMC site (106.0 ± 22.4 s $m^{-1}$) was even comparable to the typical daytime $R_c$ over forests (Fig. 3c), which was the lowest resistance due to effective stomatal uptake of ozone by leaves. The nighttime $R_{soil}$, with a mean of 159.5 ± 30.7 s $m^{-1}$, was approximately 0.5 times higher than the daytime $R_{soil}$, but still remained the lowest in literature.[33] Such diel structure of $R_{soil}$ at NMC site was also worthy of highlighting. In comparison, the nighttime $R_c$ on forest canopies was generally 1.5 times (sometimes up to 10 times) higher than the daytime $R_c$ due to the closure of leaf stomata.[27] Mechanism exploration and parameterization of $R_{soil}$ will be discussed in next section. A comparison of daytime $R_a$ + $R_b$ at NMC site (62.3 ± 15.8 s $m^{-1}$) with previous studies in various environments (56.5 ± 25.7 s $m^{-1}$) indicated efficient atmospheric turbulent transport at NMC site (Fig. 3b). A much smaller nighttime $R_a$ + $R_b$ here (110.4 ± 15.3 s $m^{-1}$ *vs.* 200.5 ± 101.0 s $m^{-1}$ in various environments) implied the more rapid ozone deposition at night as well. $R_a$ + $R_b$ is reasonably well defined and can be expressed by a function of $u_*$ and $z/L$ (eqn (6) and (7)), which are affected by WS and $R_g$. Strong WS and $R_g$ at NMC site allow neither a high $R_a$ + $R_b$ nor a very low $R_a$ + $R_b$ due to the insensitive response of $R_a$ + $R_b$ to WS at its high value end.

Similar to previous impressions, $R_{soil}$ is the major fraction (62 ± 7%) of $R_{all}$ during both the daytime and the nighttime, suggesting $R_{soil}$ plays the dominant role in ozone deposition at NMC site. The low $R_{soil}$ and $R_a$ + $R_b$ together explain large $v_d$ in both daytime and nighttime. The spatial variability in $R_{soil}$ and $v_d$ over different climates across 3 orders of magnitude (Fig. 3c and S3†), whereas the span range of $R_{soil}$ at NMC site is the smallest and distributed at the lower end of reported $R_{soil}$. To date, our study reported the only observation of $R_{soil}$ in highland climate regions, and the significant differences from previous studies highlighted the heterogeneity of $R_{soil}$ over different climates.

### 3.3 Variability of $R_{soil}$ and its parameterization

In-depth understanding of soil uptake of ozone could help to establish a more robust empirical parameterization of $R_{soil}$. Clifton *et al.*[27] proposed a mechanistic model of $R_{soil}$, which represents ozone reaction with soil surfaces and gases in soil pore spaces. Although it is tough to measure all of the parameters required for the mechanistic model in a field observation, it provides a roadmap to identify key parameters that control $R_{soil}$. Both the mechanistic model and previous observations[34–37] have found that moisture and temperature are two key parameters that control the temporal variability of $R_{soil}$.

Moisture is suggested a major influencing factor of $R_{soil}$ based on both mechanical deduction and observations.[27,34,37] The inhibition of soil ozone uptake by moisture is reflected in two ways.[34] First, soil moisture can block the diffusion of ozone in soil. Second, water molecules can be adsorbed by soil and occupy the reactive surface site, thus competing with ozone absorption and reactive uptake. The

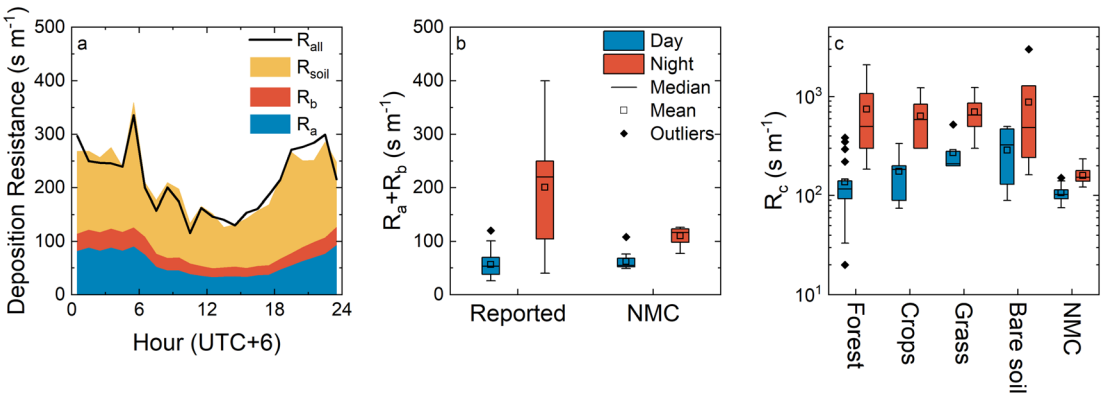


Fig. 3 (a) Median diel pattern of deposition resistance of observation at NMC site. Hourly medians are utilized instead of hourly means due to the skewed distribution of $R_{all}$ and $R_{soil}$. (b) Comparison of $R_a$ + $R_b$ and reported $R_a$ + $R_b$ during day and night. (c) Comparison of observed $R_{soil}$ and reported $R_c$ over different conditions during day and night. Parts of reported $R_c$ are obtained by $1/v_d$ minus prescribed $R_a$ + $R_b$ (50 s m$^{-1}$ during daytime and 200 s m$^{-1}$ during nighttime). Data from.[24,26,58–67]

two mechanisms account for a positive dependence of $R_{soil}$ on moisture as widely observed in field observations and laboratory experiments.[27] Our observation at NMC site also showed a significant positive dependence of $R_{soil}$ on $RH_{surf}$ (Fig. 4a). The dry climate at NMC site is conducive to keeping $R_{soil}$ small.

Temperature is a positive-going parameter for ozone uptake, as the reaction of ozone on the surface is endothermic. Thus, $R_{soil}$ decreases with increasing temperature. The mechanical deduction requires an Arrhenius-like response of $R_{soil}$ to temperature, which is verified in field observations but with large fitting uncertainty and variability.[34–36] The negative relationship between $R_{soil}$ and temperature was also observed at NMC site (Fig. 4b). Notably, the dependence of $R_{soil}$ on temperature could be a misconception due to the highly negative correlation between temperature and moisture. As a result, it is difficult to distinguish the individual effect of temperature from $RH_{surf}$ on $R_{soil}$. Nevertheless, high $T_{surf}$ is conducive to lower $R_{soil}$.

As shown in Fig. 5a and b, $R_{soil}$ can be described by an exponential equation of $RH_{surf}$ and an Arrhenius-like function of $T_{surf}$ (eqn (20) and (21)):

$$R_{soil} = 71.0 \times e^{0.012 \times RH_{surf}} \quad (20)$$

$$R_{soil} = 0.52 \times e^{\frac{12850}{RT_{surf}}} \quad (21)$$

These two parameterization schemes were tested by simulating $v_d$ with observation-constrained meteorological data by employing eqn (5)–(7) (Fig. 5c). Similar results of $v_d$ are obtained from the two parameterization schemes and both results are closely comparable to the observed $v_d$ in terms of both the magnitude and the temporal variability. Stella *et al.*[34] have found that the parameterization scheme with $RH_{surf}$ performed more robustly than the parameterization scheme with $T_{surf}$. A potential reason for this could be that $RH_{surf}$ itself contains the influence of $T_{surf}$ due to the high correlation between $RH_{surf}$ and $T_{surf}$, as previously mentioned. Herein, we choose the

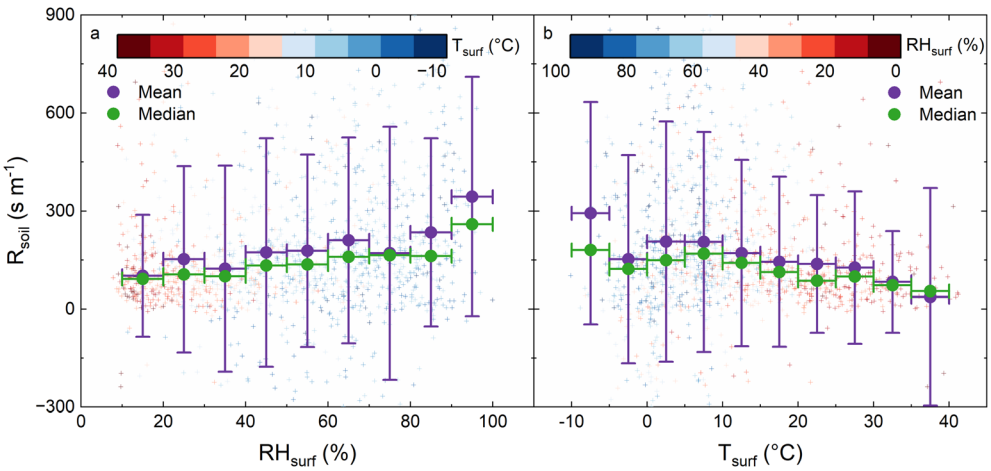


Fig. 4 Dependence of $R_{soil}$ on (a) $RH_{surf}$ and (b) $T_{surf}$. The block processing ranges of means and medians of $RH_{surf}$ and $T_{surf}$ are 10% and 5 °C, respectively.

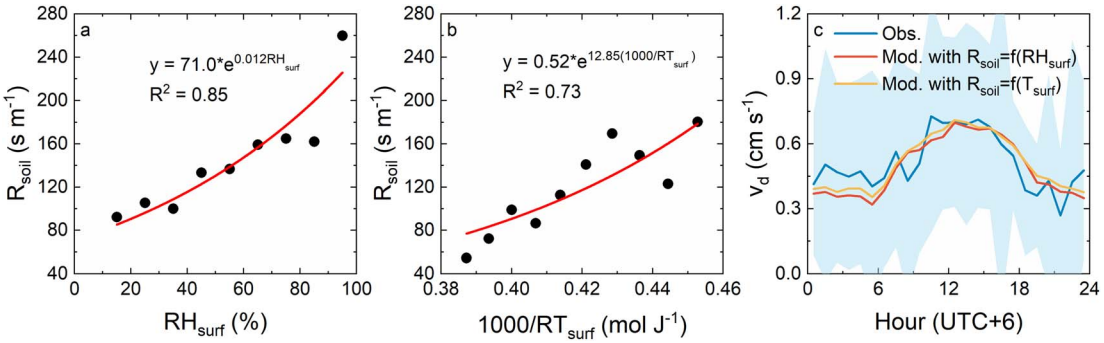


Fig. 5 $R_{soil}$ as a function of (a) $RH_{surf}$ and (b) $T_{surf}$. Dots are block median data with ranges of 10% for $RH_{surf}$ and 5 °C for $T_{surf}$. (c) Comparison of observed $v_d$ and simulated $v_d$ using $R_{soil}$ as a function of $RH_{surf}$ and $T_{surf}$ with input meteorological data from observations. The shading area for observation represents 1 sd of observed $v_d$. Time alignments are performed on the data used for comparison.

parameterization scheme with $RH_{surf}$ for further discussion. According to eqn (20), $R_{soil}$ is predicted to be lower than 240 s $m^{-1}$ at NMC site even at a high $RH_{surf}$ range, which explains the rapid ozone deposition at night. In addition, strong solar radiation and dry conditions during the daytime maintain high $T_{surf}$ and low $RH_{surf}$, which are also conducive to low $R_{soil}$.

Block medians instead of block means of $R_{soil}$ were chosen to fit the function among $R_{soil}$ and $RH_{surf}$ (or $T_{surf}$) in this study, since $R_{soil}$ at NMC was positively skewed. The fitting function based on block medians turned out to better reproduce our observations than that based on block means (Fig. 5 and S4†). As a matter of fact, $R_{soil}$ is consistently found to be positively skewed.[26,65,67,68] Thus, it needs more attention about whether the function among $R_{soil}$ and $RH_{surf}$ (or $T_{surf}$) are fitted with block medians or block means. Block means of $R_{soil}$ were used in the establishment of the Stella scheme,[33,34] which should be further examined.

### 3.4 Evaluation and improvement of the Stella scheme

$RH_{surf}$ explains the variability of $R_{soil}$ at specific sites, while soil clay content determines the site-by-site variability by affecting $R_{soil\ min}$ and $k$. According to the fitted results in eqn (20), $R_{soil\ min}$ and $k$ of NMC are 71.0 s $m^{-1}$ and 0.012, respectively. We applied the Stella scheme reversely (eqn (17)–(19)) and derived $R_{soil\ min}$ = 51.0 s $m^{-1}$ and $k$ = 0.017 at NMC. Compared with the observed $R_{soil\ min}$ (71.0 s $m^{-1}$) and $k$ (0.012), the Stella scheme underestimated $R_{soil\ min}$ by 28% and overestimated $k$ by 42% (red dots in Fig. 6a and b). By including our observations on $R_{soil\ min}$ and $k$, we updated the Stella scheme (hereafter called the updated Stella scheme, eqn (17), (20) and (21). To be noted, observations at La Crau were not included fitting in both the Stella scheme and the updated Stella scheme due to the reason mentioned in Stella *et al.*,[33] where the reported soil clay content is not representative.

$$R_{soil\ min} = 661 \times (\text{clay content})^{-0.86} \quad (22)$$

$$k = 0.0093\, e^{0.0325\times(\text{clay content})} \quad (23)$$

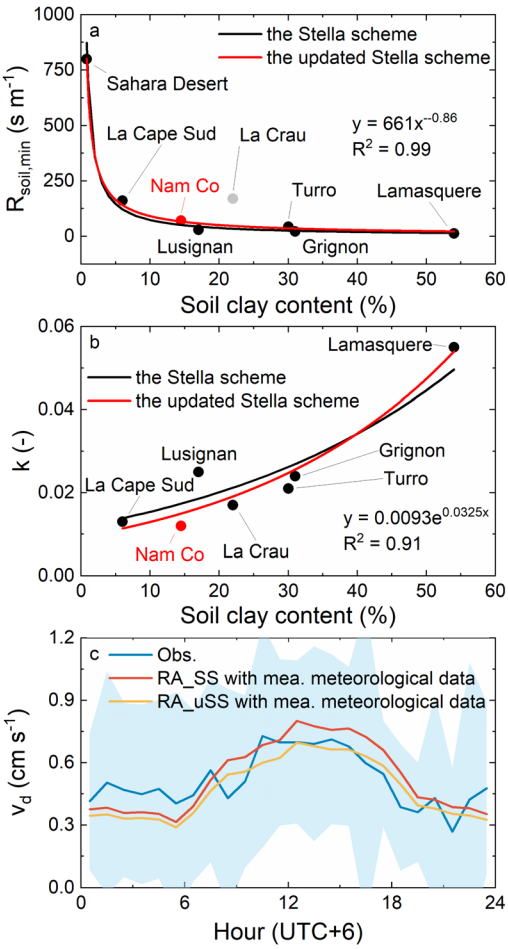


Fig. 6 Relationships between soil clay content and two coefficients in the Stella scheme, (a) minimum soil resistance ($R_{soil\ min}$) and (b) $k$. The black dots are values collected from previous observations, and the red dots are values from our observation at NMC site. The Stella scheme are shown as black lines, and the updated Stella scheme are shown as red lines. (c) Comparison of observed $v_d$ and simulated $v_d$ using the RA_SS and resistance analogy with the updated Stella scheme (RA_uSS) with input meteorological data from observations. Time alignments are performed on the data used for comparison.

The updated Stella scheme of course improved the scheme representation of $R_{soil}$ at NMC, relative to the Stella scheme. The simulation error of $R_{soil\ min}$ and $k$ was reduced from 28% and 42% to 7% and 25%. A better representative $R_{soil}$ led to a better representation of $v_d$ (Fig. 6c). The resistance analogy with the updated Stella scheme (RA_uSS) reproduced the observed daytime mean of $v_d$ of 0.58 cm $s^{-1}$. Almost the same diel pattern of $v_d$ was modelled by the RA_SS and overestimated daytime $v_d$ by only 14%. Our observations validate the feasibility of the Stella scheme and illustrate the need to include more observations in the Stella scheme.

The above analysis suggests that $v_d$ is sensitive to both $R_{soil\ min}$ and $k$. Assuming ±25% spread in $R_{soil\ min}$ and $k$, the spread in daytime and nighttime $v_d$ are calculated by the RA_uSS with typical $RH_{surf}$ (40% during daytime and 80% during nighttime) and $R_a + R_b$ (50 s $m^{-1}$ during daytime and 200 s $m^{-1}$ during nighttime). $v_d$ generally varied in a narrow range responding to $R_{soil\ min}$ changes across the entire soil clay content range (Fig. 7a). The sensitivity of $v_d$ to $k$ increases exponentially with increasing clay content (Fig. 7b). In the high soil clay content range, the ±25% spread in $k$ could cause more than 200% change in $v_d$. The sensitivity of $v_d$ to $k$ also increases with $RH_{surf}$. As a result, nighttime $v_d$ is more sensitive than daytime $v_d$ for a much higher $RH_{surf}$ range over the night. Therefore, observation verification on high soil clay contents and high $RH_{surf}$ are especially useful, though all observation verifications on varied climatic environments worthy to be highlighted, for the sake of continuous test and improvement of the updated Stella scheme.

### 3.5 Implications of the updated Stella scheme

The updated Stella scheme provides a comprehensive view of the distributions of $R_{soil}$ and $v_d$ over soil in various soil and hydrothermal conditions (Fig. 8). The rough range of soil clay content and hydrothermal conditions in different climates are also performed in Fig. 8a and b. A commonly used $R_{soil}$ in CTMs (black solid line in Fig. 8a) overestimates $R_{soil}$ in most climate regions and thus causes the underestimation of $v_d$ over soil (black solid line in Fig. 8b). And the great variability of $R_{soil}$ and $v_d$ over soil among different climate regions are not reproduced.

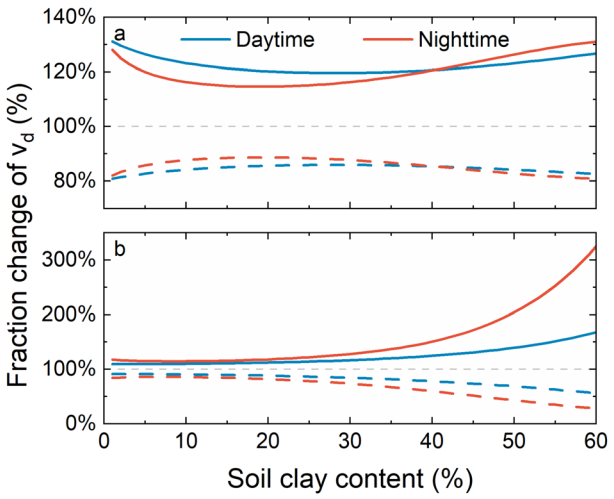


Fig. 7 Sensitivity test of daytime and nighttime $v_d$ responding to a ±25% spread (−25% and +25% change are shown in solid lines and dash lines, respectively) in (a) $R_{soil\ min}$ or (b) $k$ as calculated by the updated Stella scheme with typical $RH_{surf}$ (40% during daytime and 80% during nighttime) and $R_a + R_b$ (50 s $m^{-1}$ during daytime and 200 s $m^{-1}$ during nighttime).

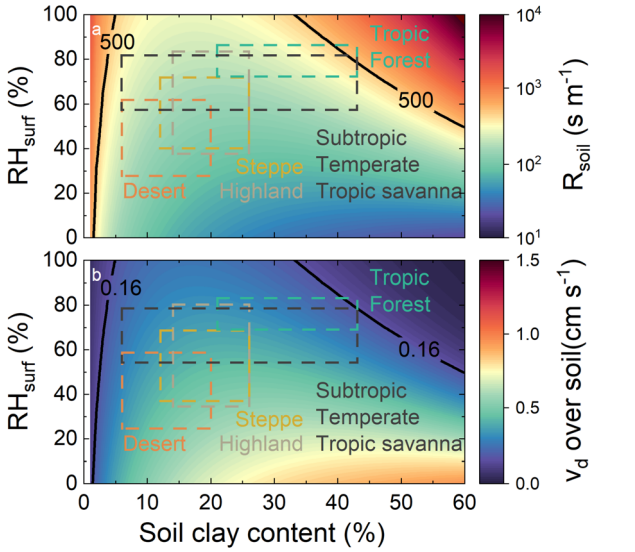


Fig. 8 Dependence of $R_{soil}$ and $v_d$ over soil on soil clay content and hydrothermal conditions. Theoretical distribution of (a) $R_{soil}$ and (b) $v_d$ over soil with different soil clay contents and $RH_{surf}$. $R_{soil}$ is calculated with the updated Stella scheme. $v_d$ is the mean of daytime and nighttime $v_d$. The daytime and nighttime $v_d$ are calculated with the assumed $R_a + R_b$ (50 s $m^{-1}$ during the daytime and 200 s $m^{-1}$ during the nighttime) and calculated $R_{soil}$. The solid black line in (a) represents a commonly used $R_{soil}$ in CTMs (500 s $m^{-1}$) and in (b) represents the $v_d$ calculated with $R_{soil}$ = 500 s $m^{-1}$. Data of climate classification and soil clay content are the same with Fig. 1. The HadISDH data[69,70] is used to estimate the approximate $RH_{surf}$ ranges of different climates.

The delineation of different climate regions in Fig. 8 is helpful to establish a general impression of the distribution of $R_{soil}$ and $v_d$ over soil in real environments. In desert, coarse soil could cause high $R_{soil\ min}$ and $R_{soil}$, and thus low $v_d$. As for tropical forest climate regions, high $RH_{surf}$ causes extremely high $R_{soil}$ and low $v_d$ over soil, thus deposition on canopy would be the major path. In vast areas of other climates, moderate soil clay content and $RH_{surf}$ supply low $R_{soil}$ and therefore high $v_d$ over soil, especially in highland climate regions and steppe. Our observation in fact provides the confirmation of high $v_d$ over soil in highland climate regions. Stella *et al.*[33] provides five observations in the subtropical climate region. More observations in different climate regions, especially in desert, steppe, and highland are needed to evaluate and improve the Stella scheme or the updated Stella scheme.

## 4 Conclusions and perspectives

This study reported the first measurement of ozone deposition in a typical highland background site with bare soil in the central TP. Unexpectedly high $v_d$ with a daily mean of 0.49 ± 0.11 cm $s^{-1}$ and an hourly mean maximum of 0.73 ± 0.67 cm $s^{-1}$ was found.

Strong solar radiation and high wind speed provided efficient turbulence energy, especially in the daytime, suggesting that atmospheric transports to the surface were not limiting steps most of the time. The soil uptake process was the main controlling process of ozone deposition at NMC. Soil uptake rate, as well as $1/R_{soil}$, was found among the top in the literature. Such high $1/R_{soil}$ was regulated by proper soil clay content, dry conditions, and strong solar radiation in the TP. These favorable conditions of soil ozone deposition are common in the TP and other highland regions. Therefore, ozone deposition in the TP and highland regions was validated as being underestimated by current models.

The Stella scheme is proven to be an effective parameterization of $R_{soil}$ by our verification at NMC site. The Stella scheme was updated through the inclusion of our observations and then better represented $R_{soil}$ and thus $v_d$ at NMC. The updated Stella scheme is recommended as a replacement for the prescribed values of $R_{soil}$ in current CTMs. Notably, both the Stella scheme and the updated Stella scheme showed the potential for continuous improvement. More quality and representative field observations of $R_{soil}$ are encouraged to further minimize the fitting uncertainty of $R_{soil\ min}$ and $k$ in the Stella scheme. Observation verifications that meet the following requirements will be helpful. First, soil deposition should be isolated from other paths of ozone deposition, such as observations over bare soils or chambers in the ground. Second, to avoid interference of reactive gases, pristine bare soils or inactivated soils are recommended. Third, perform measurements under different climatic environments to obtain different combinations of soil clay content and hydrothermal conditions. Finally, long-term and even year-round observations should be conducted to obtain a wider range of variations in the combination of $RH_{surf}$ and $T_{surf}$.

## Author contributions

Chong Zhang: data curation, formal analysis, investigation, methodology, software, visualization, writing – original draft, writing – review & editing; Jianshu Wang: investigation, writing – review & editing; Yingjie Zhang: conceptualization, funding acquisition, investigation, methodology, project administration, writing – review & editing; Wanyun Xu: data curation, investigation, writing – review & editing; Gen Zhang: investigation, writing – review & editing; Guofang Miao: software, writing – review & editing; Jiacheng Zhou: investigation, writing – review & editing; Hui Yu: investigation, writing – review & editing; Weixiong Zhao: writing – review & editing; Weili Lin: writing – review & editing; Ling Kang: resources, writing – review & editing; Xuhui Cai: writing – review & editing; Hongsheng Zhang: writing – review & editing; Chunxiang Ye: conceptualization, funding acquisition, investigation, methodology, project administration, resources, supervision, writing – review & editing.

## Conflicts of interest

There are no conflicts to declare.

## Acknowledgements

This work was supported by the Second Tibetan Plateau Scientific Expedition and Research Program (2019QZKK060604) and the National Natural Science Foundation of China (grants no. 42105110).The authors acknowledge all researchers involved in the @Tibet 2019 campaign. Thanks for the support from the Nam Co Comprehensive Observation and Research Station of Chinese Academy of Sciences.

## References

1 E. A. Ainsworth, C. R. Yendrek, S. Sitch, W. J. Collins and L. D. Emberson, *Annu. Rev. Plant Biol.*, 2012, **63**, 637–661.
2 T.-M. Fu and H. Tian, *Curr. Pollut. Rep.*, 2019, **5**, 159–171.
3 N. E. Grulke and R. L. Heath, *Plant Biol.*, 2020, **22**, 12–37.
4 M. Jerrett, R. T. Burnett, C. Arden Pope, K. Ito, G. Thurston, D. Krewski, Y. Shi, E. Calle and M. Thun, *N. Engl. J. Med.*, 2009, **360**, 1085–1095.
5 M. G. Schultz, S. Schröder, O. Lyapina, O. R. Cooper, I. Galbally, I. Petropavlovskikh, E. von Schneidemesser, H. Tanimoto, Y. Elshorbany, M. Naja, R. J. Seguel, U. Dauert, P. Eckhardt, S. Feigenspan, M. Fiebig, A.-G. Hjellbrekke, Y.-D. Hong, P. C. Kjeld, H. Koide, G. Lear, D. Tarasick, M. Ueno, M. Wallasch, D. Baumgardner, M.-T. Chuang, R. Gillett, M. Lee, S. Molloy, R. Moolla, T. Wang, K. Sharps, J. A. Adame, G. Ancellet, F. Apadula, P. Artaxo, M. E. Barlasina, M. Bogucka, P. Bonasoni, L. Chang, A. Colomb, E. Cuevas-Agulló, M. Cupeiro, A. Degorska, A. Ding, M. Fröhlich, M. Frolova, H. Gadhavi, F. Gheusi, S. Gilge, M. Y. Gonzalez, V. Gros, S. H. Hamad, D. Helmig, D. Henriques, O. Hermansen, R. Holla, J. Hueber, U. Im, D. A. Jaffe, N. Komala, D. Kubistin, K.-S. Lam, T. Laurila, H. Lee, I. Levy, C. Mazzoleni, L. R. Mazzoleni, A. McClure-Begley, M. Mohamad, M. Murovec, M. Navarro-Comas, F. Nicodim, D. Parrish, K. A. Read, N. Reid, L. Ries, P. Saxena, J. J. Schwab, Y. Scorgie, I. Senik, P. Simmonds, V. Sinha, A. I. Skorokhod, G. Spain, W. Spangl, R. Spoor, S. R. Springston, K. Steer, M. Steinbacher, E. Suharguniyawan, P. Torre, T. Trickl, L. Weili, R. Weller, X. Xiaobin, L. Xue and M. Zhiqiang, *Elem. Sci. Anth.*, 2017, **5**, 58.
6 A. T. Archibald, J. L. Neu, Y. F. Elshorbany, O. R. Cooper, P. J. Young, H. Akiyoshi, R. A. Cox, M. Coyle, R. G. Derwent, M. Deushi, A. Finco, G. J. Frost, I. E. Galbally, G. Gerosa, C. Granier, P. T. Griffiths, R. Hossaini, L. Hu, P. Jöckel, B. Josse, M. Y. Lin, M. Mertens, O. Morgenstern, M. Naja, V. Naik, S. Oltmans, D. A. Plummer, L. E. Revell, A. Saiz-Lopez, P. Saxena, Y. M. Shin, I. Shahid, D. Shallcross, S. Tilmes, T. Trickl, T. J. Wallington, T. Wang, H. M. Worden and G. Zeng, *Elementa*, 2020, **8**, 1–53.
7 O. E. Clifton, F. Paulot, A. M. Fiore, L. W. Horowitz, G. Correa, C. B. Baublitz, S. Fares, I. Goded, A. H. Goldstein, C. Gruening, A. J. Hogg, B. Loubet, I. Mammarella, J. W. Munger, L. Neil, P. Stella, J. Uddling,

T. Vesala and E. Weng, *J. Geophys. Res.: Atmos.*, 2020, **125**, e2020JD032398.
8 A. Y. H. Wong, J. A. Geddes, A. P. K. Tai and S. J. Silva, *Atmos. Chem. Phys.*, 2019, **19**, 14365–14385.
9 D. Simpson, *Atmos. Environ., Part A*, 1992, **26**, 1609–1634.
10 J.-T. Lin, D. Youn, X.-Z. Liang and D. J. Wuebbles, *Atmos. Environ.*, 2008, **42**, 8470–8483.
11 S. Solberg, Ø. Hov, A. Søvde, I. S. A. Isaksen, P. Coddeville, H. De Backer, C. Forster, Y. Orsolini and K. Uhse, *J. Geophys. Res.: Atmos.*, 2008, **113**(D7), DOI: 10.1029/2007JD009098.
12 M. L. Wesely, *Atmos. Environ.*, 1989, **23**, 1293–1304.
13 T. Emmerichs, A. Kerkweg, H. Ouwersloot, S. Fares, I. Mammarella and D. Taraborrelli, *Geosci. Model Dev.*, 2021, **14**, 495–519.
14 S. Falk and A. Søvde Haslerud, *Geosci. Model Dev.*, 2019, **12**, 4705–4728.
15 I. Lagzi, R. Mészáros, L. Horváth, A. Tomlin, T. Weidinger, T. Turányi, F. Ács and L. Haszpra, *Atmos. Environ.*, 2004, **38**, 6211–6222.
16 R. J. Park, S. K. Hong, H.-A. Kwon, S. Kim, A. Guenther, J.-H. Woo and C. P. Loughner, *Atmos. Chem. Phys.*, 2014, **14**, 7929–7940.
17 L. Zhang, J. R. Brook and R. Vet, *Atmos. Chem. Phys.*, 2003, **3**, 2067–2082.
18 S. Galmarini, P. Makar, O. E. Clifton, C. Hogrefe, J. O. Bash, R. Bellasio, R. Bianconi, J. Bieser, T. Butler, J. Ducker, J. Flemming, A. Hodzic, C. D. Holmes, I. Kioutsioukis, R. Kranenburg, A. Lupascu, J. L. Perez-Camanyo, J. Pleim, Y.-H. Ryu, R. San Jose, D. Schwede, S. Silva and R. Wolke, *Atmos. Chem. Phys.*, 2021, **21**, 15663–15697.
19 Z. Wu, D. B. Schwede, R. Vet, J. T. Walker, M. Shaw, R. Staebler and L. Zhang, *J. Adv. Model. Earth Syst.*, 2018, **10**, 1571–1586.
20 D. Schwede, L. Zhang, R. Vet and G. Lear, *Atmos. Environ.*, 2011, **45**, 1337–1346.
21 E. Lamaud, A. Carrara, Y. Brunet, A. Lopez and A. Druilhet, *Atmos. Environ.*, 2002, **36**, 77–88.
22 K. F. Zeller and N. T. Nikolov, *Environ. Pollut.*, 2000, **107**, 1–20.
23 S. Fares, F. Savi, J. Muller, G. Matteucci and E. Paoletti, *Agric. For. Meteorol.*, 2014, **198–199**, 181–191.
24 K. Matsuda, I. Watanabe, V. Wingpud, P. Theramongkol, P. Khummongkol, S. Wangwongwatana and T. Totsuka, *Atmos. Environ.*, 2005, **39**, 2571–2577.
25 A. J. Visser, L. N. Ganzeveld, I. Goded, M. C. Krol, I. Mammarella, G. Manca and K. F. Boersma, *Atmos. Chem. Phys.*, 2021, **21**, 18393–18411.
26 M. Coyle, E. Nemitz, R. Storeton-West, D. Fowler and J. N. Cape, *Agric. For. Meteorol.*, 2009, **149**, 655–666.
27 O. E. Clifton, A. M. Fiore, W. J. Massman, C. B. Baublitz, M. Coyle, L. Emberson, S. Fares, D. K. Farmer, P. Gentine, G. Gerosa, A. B. Guenther, D. Helmig, D. L. Lombardozzi, J. W. Munger, E. G. Patton, S. E. Pusede, D. B. Schwede, S. J. Silva, M. Sörgel, A. L. Steiner and A. P. K. Tai, *Rev. Geophys.*, 2020, **58**, e2019RG000670.
28 L. Horváth, P. Koncz, A. Móring, Z. Nagy, K. Pintér and T. Weidinger, *Bound. -Layer Meteorol.*, 2017, **167**, 303–326.
29 P. Stella, E. Personne, E. Lamaud, B. Loubet, I. Trebs and P. Cellier, *J. Geophys. Res.: Biogeosci.*, 2013, **118**, 1120–1132.
30 E. Lamaud, B. Loubet, M. Irvine, P. Stella, E. Personne and P. Cellier, *Agric. For. Meteorol.*, 2009, **149**, 1385–1396.
31 S. J. Silva and C. L. Heald, *J. Geophys. Res.: Atmos.*, 2018, **123**, 559–573.
32 P. Stella, E. Personne, B. Loubet, E. Lamaud, E. Ceschia, P. Béziat, J. M. Bonnefond, M. Irvine, P. Keravec, N. Mascher and P. Cellier, *Biogeosciences*, 2011, **8**, 2869–2886.
33 P. Stella, B. Loubet, C. de Berranger, X. Charrier, E. Ceschia, G. Gerosa, A. Finco, E. Lamaud, D. Serça, C. George and R. Ciuraru, *Atmos. Environ.*, 2019, **199**, 202–209.
34 P. Stella, B. Loubet, E. Lamaud, P. Laville and P. Cellier, *Agric. For. Meteorol.*, 2011, **151**, 669–681.
35 J. N. Cape, R. Hamilton and M. R. Heal, *Atmos. Environ.*, 2009, **43**, 1116–1123.
36 I. Fumagalli, C. Gruening, R. Marzuoli, S. Cieslik and G. Gerosa, *Agric. For. Meteorol.*, 2016, **228–229**, 205–216.
37 W. J. Massman, *Atmos. Environ.*, 2004, **38**, 2323–2337.
38 S. Bassin, P. Calanca, T. Weidinger, G. Gerosa and J. Fuhrer, *Atmos. Environ.*, 2004, **38**, 2349–2359.
39 D. Chen and H. W. Chen, *Environ. Dev.*, 2013, **6**, 69–79.
40 FAO and IIASA, *Harmonized World Soil Database version 2.0*, 2023.
41 M. Kummu, M. Heino, M. Taka, O. Varis and D. Viviroli, *One Earth*, 2021, **4**, 720–729.
42 P. Stella, B. Loubet, P. Laville, E. Lamaud, M. Cazaunau, S. Laufs, F. Bernard, B. Grosselin, N. Mascher, R. Kurtenbach, A. Mellouki, J. Kleffmann and P. Cellier, *Atmos. Meas. Tech.*, 2012, **5**, 1241–1257.
43 R. M. Vuolo, B. Loubet, N. Mascher, J. C. Gueudet, B. Durand, P. Laville, O. Zurfluh, R. Ciuraru, P. Stella and I. Trebs, *Biogeosciences*, 2017, **14**, 2225–2244.
44 J. Wang, Y. Zhang, C. Zhang, Y. Wang, J. Zhou, L. K. Whalley, E. J. Slater, J. E. Dyson, W. Xu, P. Cheng, B. Han, L. Wang, X. Yu, Y. Wang, R. Woodward-Massey, W. Lin, W. Zhao, L. Zeng, Z. Ma, D. E. Heard and C. Ye, *Environ. Sci. Technol.*, 2023, **57**, 5474–5484.
45 X. Xu, H. Zhang, W. Lin, Y. Wang, W. Xu and S. Jia, *Atmos. Chem. Phys.*, 2018, **18**, 5199–5217.
46 X. Yin, S. Kang, B. de Foy, Z. Cong, J. Luo, L. Zhang, Y. Ma, G. Zhang, D. Rupakheti and Q. Zhang, *Atmos. Chem. Phys.*, 2017, **17**, 11293–11311.
47 W. Lin, X. Xu, X. Zheng, J. Dawa, C. Baima and J. Ma, *J. Environ. Sci.*, 2015, **31**, 133–145.
48 J. Huang, S. Kang, Q. Zhang, H. Yan, J. Guo, M. G. Jenkins, G. Zhang and K. Wang, *Atmos. Environ.*, 2012, **62**, 540–550.
49 L. Wang, C. Yi, X. Xu, B. Schütt, K. Liu and L. Zhou, *J. Mt. Sci.*, 2009, **6**, 354–361.
50 B. Fang, W. Zhao, X. Xu, J. Zhou, X. Ma, S. Wang, W. Zhang, D. S. Venables and W. Chen, *Opt. Express*, 2017, **25**, 26910.
51 Z. Y. Wu, L. Zhang, X. M. Wang and J. W. Munger, *Atmos. Chem. Phys.*, 2015, **15**, 7487–7496.

52 M. Mauder, M. Cuntz, C. Drüe, A. Graf, C. Rebmann, H. P. Schmid, M. Schmidt and R. Steinbrecher, *Agric. For. Meteorol.*, 2013, **169**, 122–135.
53 N. Kljun, P. Calanca, M. W. Rotach and H. P. Schmid, *Bound. -Layer Meteorol.*, 2004, **112**, 503–523.
54 S. Walton, M. W. Gallagher and J. H. Duyzer, *Atmos. Environ.*, 1997, **31**, 2915–2931.
55 V. Wolff, I. Trebs, T. Foken and F. X. Meixner, *Biogeosciences*, 2010, **7**, 1729–1744.
56 J. Rinne, J.-P. Tuovinen, T. Laurila, H. Hakola, M. Aurela and H. Hypén, *Agric. For. Meteorol.*, 2000, **102**, 25–37.
57 A. Ito and R. Wagai, *Sci. Data*, 2017, **4**, 170103.
58 S. Cieslik, *Environ. Pollut.*, 2009, **157**, 1487–1496.
59 R. Wada, S. Yonemura, A. Tani and M. Kajino, *J. Agric. Meteorol.*, 2023, **79**, 38–48.
60 D. Fowler, C. Flechard, J. N. Cape, R. L. Storeton-West and M. Coyle, *Water, Air, Soil Pollut.*, 2001, **130**, 63–74.
61 G. Gerosa, R. Marzuoli, S. Cieslik and A. Ballarin-Denti, *Atmos. Environ.*, 2004, **38**, 2421–2432.
62 T. P. Meyers, P. Finkelstein, J. Clarke, T. G. Ellestad and P. F. Sims, *J. Geophys. Res.: Atmos.*, 1998, **103**, 22645–22661.
63 M. Michou, P. Laville, D. Serça, A. Fotiadi and V.-H. Peuch, *Atmos. Res.*, 2005, **74**, 89–116.
64 T. N. Mikkelsen, H. Ro-Poulsen, M. F. Hovmand, N. O. Jensen, K. Pilegaard and A. H. Egeløv, *Atmos. Environ.*, 2004, **38**, 2361–2371.
65 C. A. Pio, M. S. Feliciano, A. T. Vermeulen and E. C. Sousa, *Atmos. Environ.*, 2000, **34**, 195–205.
66 M. Zapletal, P. Cudlín, P. Chroust, O. Urban, R. Pokorný, M. Edwards-Jonášová, R. Czerný, D. Janouš, K. Taufarová, Z. Večeřa, P. Mikuška and E. Paoletti, *Environ. Pollut.*, 2011, **159**, 1024–1034.
67 L. Zhang, J. R. Brook and R. Vet, *Atmos. Environ.*, 2002, **36**, 4787–4799.
68 L. Zhang, M. D. Moran, P. A. Makar, J. R. Brook and S. Gong, *Atmos. Environ.*, 2002, **36**, 537–560.
69 K. M. Willett, R. J. H. Dunn, P. W. Thorne, S. Bell, M. de Podesta, D. E. Parker, P. D. Jones and C. N. Williams Jr, *Clim. Past*, 2014, **10**, 1983–2006.
70 A. Smith, N. Lott and R. Vose, *Bull. Am. Meteorol. Soc.*, 2011, **92**, 704–708.